Proceedings of the ASME 2025
Verification, Validation, and Uncertainty Quantification Symposium
VVUQ2025
April 9-11, College Station, TX, USA

VVUQ2025-151136

USING 3D MEASUREMENTS FROM MRI TO IMPROVE VVUQ

Michael Benson[1], Thien Nguyen[1], Daniel Borup[2]

[1]Oak Ridge National Laboratory, Oak Ridge, TN
[2]Borup Solutions, Rochester, MN

ABSTRACT

Magnetic resonance velocimetry (MRV) is a diagnostic that can measure 3D, three-component turbulent velocity fields in arbitrarily complex flow configurations. The approach uses magnetic resonance imaging (MRI), which is a system commonly available in radiology departments or medical research centers. MRV acquires signal from hydrogen protons in water channel flows. Despite the obvious utility of the measurements for investigating a variety of flows, comparisons with computational fluid dynamic (CFD) simulations largely retain traditional metrics, comparing velocity profiles and planes at discrete regions within the flow rather than using the 3D nature of the measured field. In this effort, MRV was conducted in a simple water channel with six spanwise-centered periodic obstacles roughly shaped as cubes. At a fully turbulent Reynolds number of 15,000, the channel includes two flows: a main streamwise flow and, in the wake of the second obstacle, an injected flow oriented perpendicular to the streamwise flow. The flow geometry includes partial obstacles on the side walls and is inherently 3D because of the interaction of the two streams and the wake features, making the flow challenging to completely measure with traditional optical techniques. Aside from line profiles and planar comparisons, two 3D metrics are used to compare the data with a steady Reynolds-averaged Navier–Stokes (RANS) simulation result. A brief discussion about the comparison is provided, including comments about uncertainty.

Keywords: MRV, validation, RANS

NOMENCLATURE

CFD	computational fluid dynamics
LPM	liters per minute
MRV	magnetic resonance velocimetry
RANS	Reynolds-averaged Navier–Stokes
Re	Reynolds number
RMSE	root mean squared error
U, *V*, *W*	velocity components in the *x*, *y*, *z* directions
VENC	velocity encode

1. INTRODUCTION

A wide variety of experimental techniques have been developed to measure the velocity field in turbulent flows. Many university curricula include courses on the topic, and the techniques can involve the insertion of probes [1] or the imaging of tracers or markers [2, 3]. Some methods are extremely fast and can resolve the smallest important time scales of the flow [4], whereas others are not, representing the time-averaged flow field [5]. Most techniques yield either point or planar measurements, although tomographic particle image velocimetry [6] is one approach that can also measure 3D fields. This work focuses on nuclear magnetic resonance and uses systems commonly found in radiology departments and research centers. MRV has been used in turbulent flow studies for several decades [7-10] and provides time-averaged 3D velocity three-component velocity fields at submillimeter resolution. However, validation criteria do not generally use 3D metrics to assess CFD results [11]. The objective of this work is to leverage the complete detail of MRV in a validation activity with a RANS simulation of a turbulent flow in a water channel apparatus.

2. MATERIALS AND METHODS

2.1 Geometry and Equipment

The geometry of interest is the same one used in the second iteration of the 2019 MRV Challenge [12]. Figure 1 depicts the 850 mm long channel with flow development sections as well as the test section where the measurements were taken. The flow development includes two honeycomb elements and six grids, as well as a 4:1 area ratio contraction to eliminate secondary flows entering the test section. The test section is square, with height H = 25 mm and length of 240 mm. The primary flow is left to right through the assembly and includes a secondary flow from the bottom of the test section through a 5 mm square opening. The flow rates are 22 and 1 liters per minute (LPM) for the two flows, respectively, yielding a mainstream Reynolds number *(Re)* based on water at 22°C and the channel hydraulic diameter

of *Re* = 15,000. A 1 mm square trip on all four channel walls 25 mm downstream of the flange ensures the flow is turbulent. Water is the working fluid with a 0.06 mol/L concentration of copper sulfate—an inexpensive contrast agent that shortens the acquisition time for the MRV sequences and does not incur appreciable differences in fluid properties at that concentration. Ice bottles were used in the reservoir to maintain the water temperature within 1°C. The six centerline obstacles are 7.5 mm cubic elements spaced 15 mm apart. Each side wall of the channel has partial obstacles extending 1.75 mm into the flow that have alternating 7.5- and 12.5-mm heights, each aligned with the cubic elements as depicted on one side in Figure 1. The streamwise coordinate is x, with y the wall normal, and z the spanwise. For MRV measurements, the coordinate origin is set to the downstream edge of the bottom of the trip in the channel, 41.5 mm upstream from the bottom center of the first cube.

The 22 LPM flow was supplied by a Finish Thompson DB6HP-M226 centrifugal pump. The 1 LPM injector flow, which is continuous and steady unlike the flow in the 2nd MRV Challenge [12], was supplied by a Little Giant 582002 4-MD magnetic drive pump. Flow rates and temperatures were monitored throughout testing using Kobold DUK-12N4HC3T00

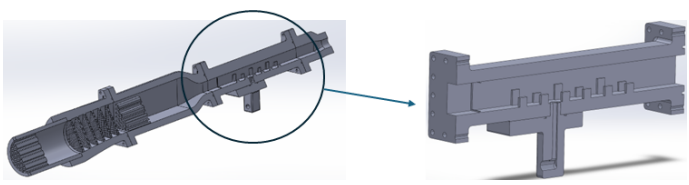

FIGURE 1: CROSS SECTIONAL VIEW OF WATER CHANNEL ASSEMBLY (*L*) WITH TEST SECTION (*R*)

meshes were generated using the automated meshing capabilities in Star-CCM+. Numerical simulations were performed using a segregated flow with RANS realizable k-ε turbulence model and two-layer all y+ wall treatment to simulate the fluid flow within the test section. Simulations using RANS k-ω SST turbulence model were also performed but are not presented here. Velocity profiles along a cross section extracted from MRV measurements were used as inlet boundary conditions for CFD simulations. For the mesh generation, the Surface Remesher, Trimmed Cell Mesher, and Prism Layer Mesher were used. The Surface Remesher performed surface vertex re-tessellate of the imported 3D CAD to optimize surface faces based on the target edge length and proximity refinements. The Trimmed Cell Mesher (hexahedra type) provides a robust and efficient method of producing a high-quality grid for both simple and complex mesh generation problems because it has highly desirable meshing attributes, such as predominantly hexahedral mesh with minimal cell skew, refinement based upon surface mesh size and other user-defined refinement controls, surface quality independence, and alignment with a user-specified coordinate system. In the Trimmed Cell Mesher, growth rates control the rate at which cell sizes increase from one cell size to another within the trimmed cell mesh. The Surface Growth Rate controls the rate of size changes between the cells that are next to surfaces and the cells in the core. The Prism Layer Mesher generated a subsurface to extrude a set of prismatic cells from region surfaces into the core mesh. This layer of cells is necessary to improve the accuracy of the flow solution. The computational meshes were generated using a base size of 1.25 mm, a surface growth rate of 1.3, and refinements to the cell sizes in the vicinity of the wall surfaces and wall layers. Prism cells were applied in nine

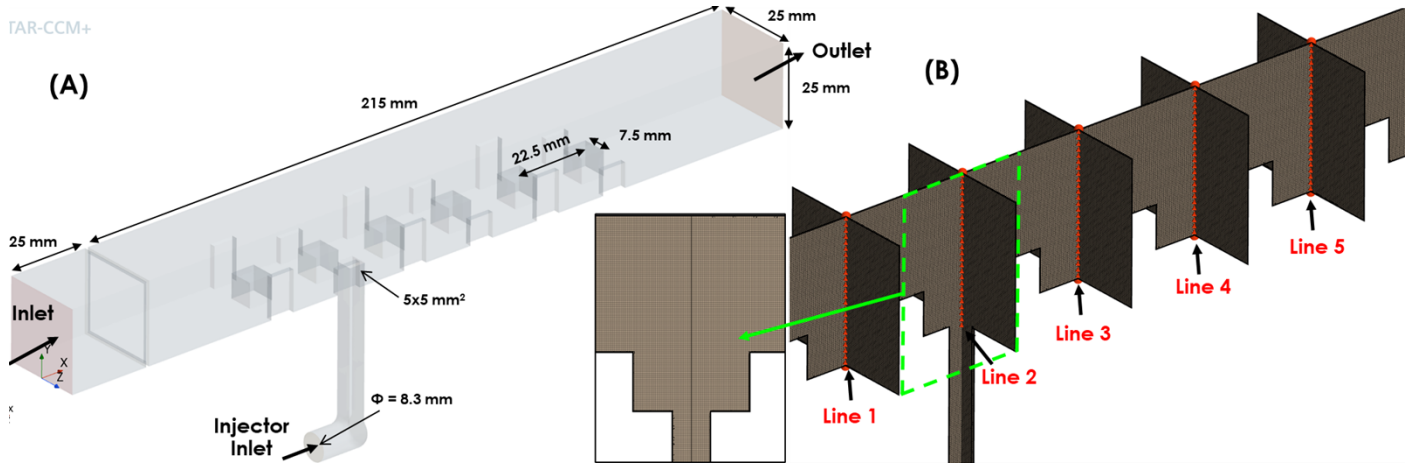

FIGURE 2: (A) COMPUTATIONAL DOMAIN, (B) FINE GRID USED FOR RANS SIMULATION

and 12NBHC3T00 flow meters for primary and injector flows, respectively.

2.2 Numerical Modeling

The CAD design of the test section was imported into the commercial CFD package Simcenter Star-CCM+ [13], and 3D

layers in the near-wall region for a total thickness of 0.18 mm, and a prism layer near-wall thickness of 0.0025 mm. The nondimensional wall distance y+ was maintained as less than 1. In addition, grid refinements were locally performed in the regions surrounding the cubes, the injector, and the plume downstream using the volume control method in the Star-CCM+

mesh generator. The sensitivity of the mesh discretization on relevant fluid flow quantities was investigated. Coarse (1.34 million cells), medium (5.11 million cells), fine (9.17 million cells), and very fine (19.26 million cells) meshes were generated. Grid sensitivity studies were based on results of fluid-flow physics calculations using the RANS realizable k-ε turbulence model. Results of the grid sensitivity studies obtained from the evaluations of mean velocity and turbulent kinetic energy profiles at several streamwise locations showed that fine mesh could be used. Results presented in this paper were acquired from the fine mesh.

2.3 MRV Scan Sequences and Uncertainty

The MRV was conducted using a Philips 3TX Elition located at the Vanderbilt University Institute for Imaging Science in Nashville, Tennessee, and running the MR7700 software (version R5.9). The Philips 16-channel head coil was used with an isotropic scan resolution of 0.7 mm through the test section, yielding a matrix size of 368 × 132 × 60 for the data. The velocity encodes (VENC) were set to 140, 120, and 84 cm/s in the streamwise (x), wall-normal (y), and spanwise (z) directions, respectively. Each scan took 2 min 45 s to complete, with the echo time at 3.0 ms and repetition time at 6.7 ms, the elliptical k-space filter option enabled, and a water-fat shift setting of 1.258 pixels, which equates to a 62.5 MHz bandwidth setting for a GE system. The MRV data were obtained by first measuring a flow-off case, and then conducting a series of three flow-on cases. Bookending flow-off cases on each side of 3 flow-on cases was conducted a total of 5 times, yielding 15 flow-on scans and 6 flow-off scans. The flow-off scans on either side of each group were averaged and subtracted from each flow-on scan to reduce errors associated with magnetic field drift and thermal effects that may vary in time with MRI utilization. For the uncertainty calculation, each individual flow-on case had an average of the two neighboring flow-off scans subtracted. The point-by-point standard deviation was then calculated across the series. The data were interrogated within a volume of interest comprising 18,000 voxels in the free stream, and the average uncertainty calculated for each velocity component as a fraction of the VENC used in the scan sequence. The calculated uncertainty was less than 3% of the VENC for all three velocity components and only 2% for U and V.

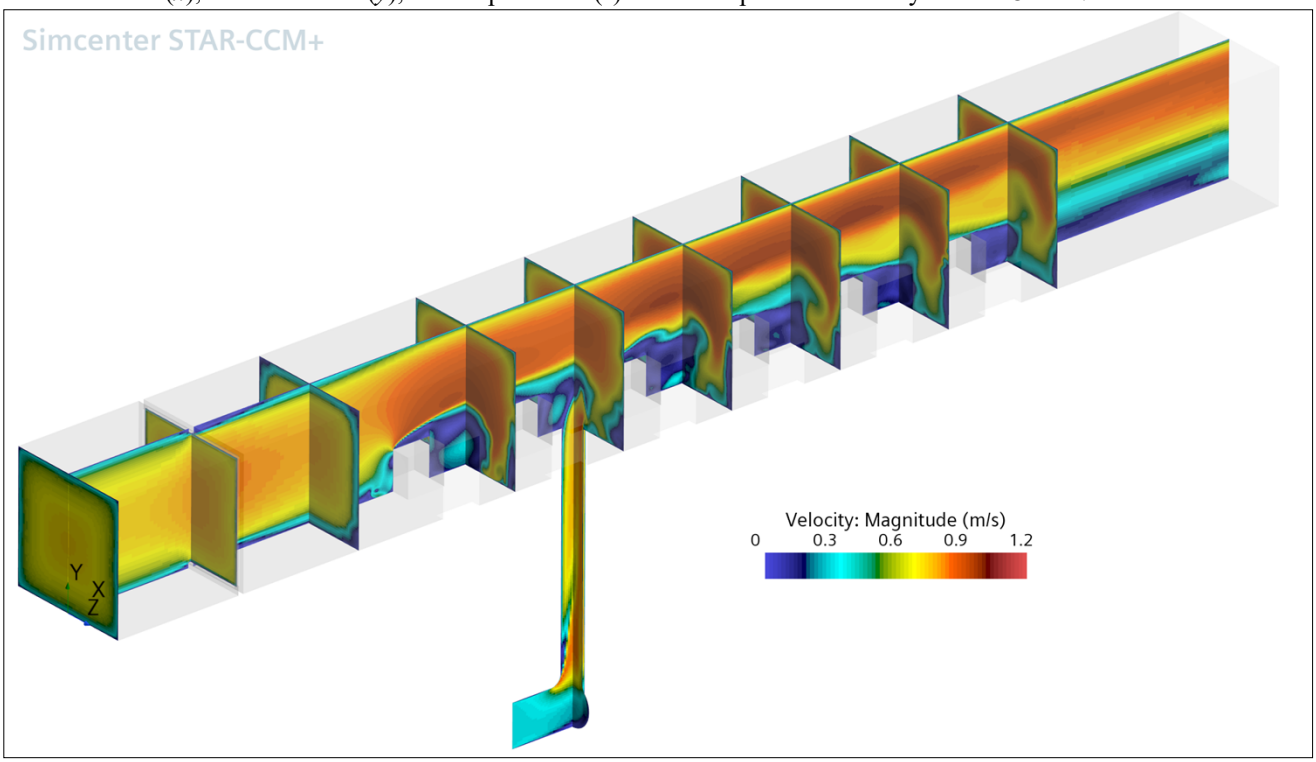

FIGURE 3: GENERAL DEPICTION OF THE VELOCITY MAGNITUDE INDICATING THE STREAMWISE AND INJECTOR FLOW ACROSS OBSTACLES FROM RANS

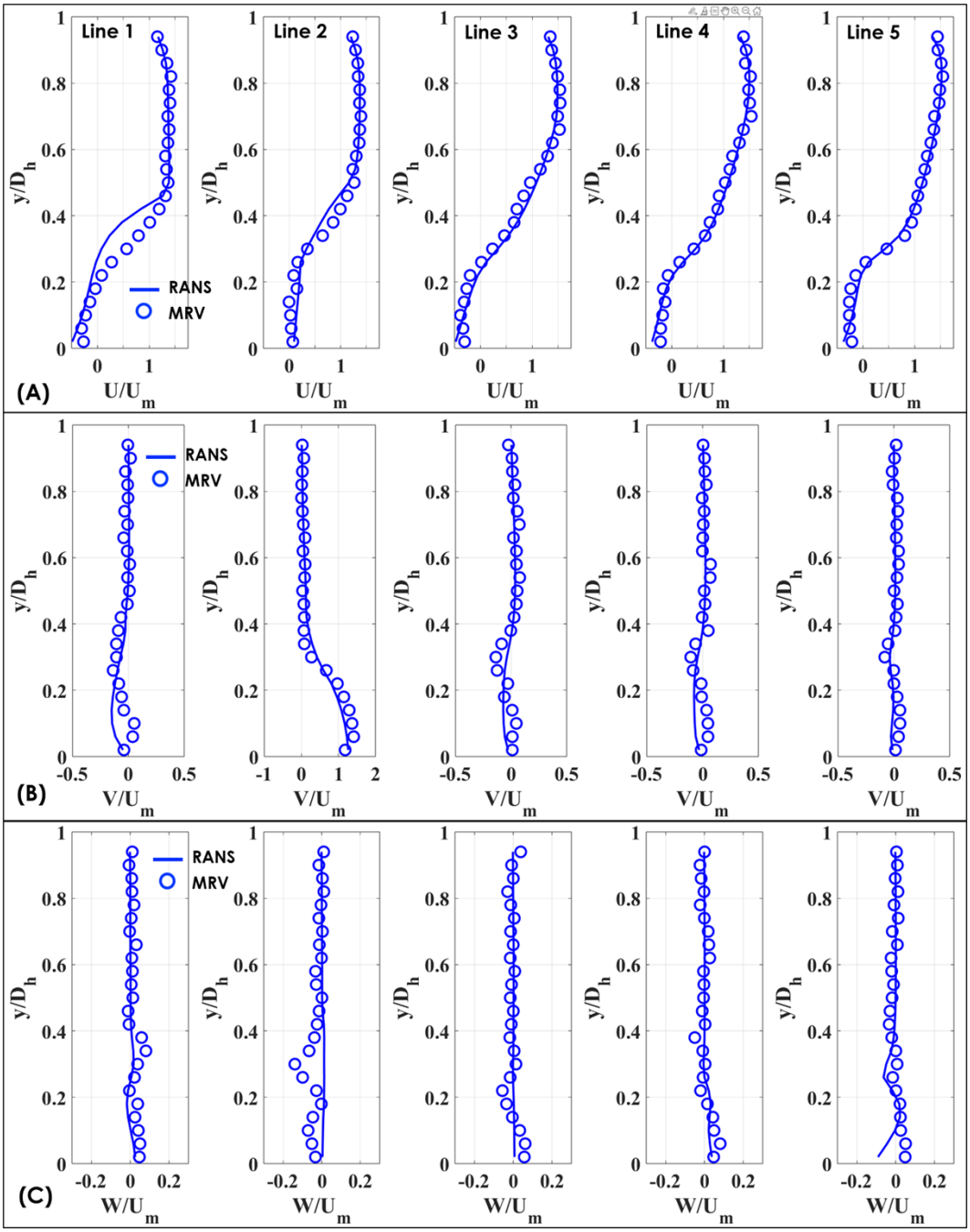

FIGURE 4: COMPARISONS RANS (—) AND MRV (O) ALONG LINES 1–5 LOCATED WITHIN THE CHANNEL CENTERPLANE. (A) STREAMWISE, U/U_m; (B) VERTICAL, V/U_m; AND (C) SPANWISE W/U_m VELOCITY COMPONENTS

3. RESULTS AND DISCUSSION

Figure 3 depicts the key features of the flow from the RANS simulation using the velocity magnitude. The free stream flow moves left to right and generally accelerates above the obstacles as it moves downstream. The channel side walls and top are hidden to aid in visualization of the field. The injector flow occurs between the second and third obstacles and interacts with the free stream and upstream obstacle wakes in a highly 3D fashion. The obstacles themselves are shown in translucent white, suggesting that the side wall interactions contribute to the complex nature of the flow physics involved. Traditional comparisons between experimental and computational results usually include line plots such as the ones depicted in Figure 4. The plots in this figure compare the mean streamwise, U, vertical, V, and spanwise, W, velocity components obtained from

MRV measurements and RANS simulations at five spatial lines (see Figure 2B) along the channel centerplane. The velocity is normalized by the bulk averaged velocity of U_m = 0.59 m/s and the channel height by D_h = 25 mm. An overall good agreement between MRV and RANS is observed, except for discrepancies of U profiles along Line 1 with $0.2 < y/D_h < 0.5$ and Line 2 with $0.3 < y/D_h < 0.5$. Comparisons of V profiles show a good agreement with $y/D_h > 0.35$ and some disagreements with $y/D_h < 0.2$ (i.e., in the recirculation flow region within two obstacles). The spanwise velocity profiles W were approximately 2 orders of magnitude smaller than the streamwise component U and comparison of RANS and MRV shows a reasonably good agreement.

An overall evaluation of the agreement between velocity profiles obtained from RANS and MRV can be performed using the equation below, which produces the RMS velocity difference between the two datasets over a given set of profiles.

$$\sigma_U = \frac{1}{NM}\sum_{i=1}^{N}\sum_{j=1}^{M}\sqrt{\overline{(U_{MRV} - U_{CFD})^2}} \qquad (1)$$

In this equation, N is the number of lines and M is the number of points along each line in the profile comparisons. In the present case N = 5 and M = 24. Applying Equation 1 to the U, V, and W profiles obtained from the MRV measurements and RANS simulations (Fig. 4) yielded the following set of normalized RMS differences for each velocity component:

$$\left[\frac{\sigma_U}{U_m}, \frac{\sigma_V}{U_m}, \frac{\sigma_W}{U_m}\right] = [12.3\%, 6.7\%, 3.5\%]. \qquad (2)$$

These statistics show that the level of agreement between the RANS and the MRV results is highest in W, where the RMS difference is near the quoted experimental uncertainty of 3%. The agreement is lowest in the streamwise velocity component, U. The values in Equation 2 can be interpreted as a quantitative assessment of the reliability of the simulation to provide the "right answer" for the velocity at these five locations within the flow. However, the profiles themselves indicate that the most challenging regions are behind the initial obstacles in the flow (e.g., profile lines 1 and 2).

To better understand the spatial agreement between the flow fields, planar comparisons can also be made. Figures 5–7 depict the three velocity components at a streamwise plane collocated with Line 2 and the injector flow as depicted in the inset image of Figure 2. Although the depictions qualitatively appear similar, it is more challenging to do quantitative comparisons although point-by-point comparisons are possible. In the case of the spanwise velocity in Figure 7, small spatial variations separate positive and negative velocities that could manifest into significant errors in those regions if not carefully addressed.

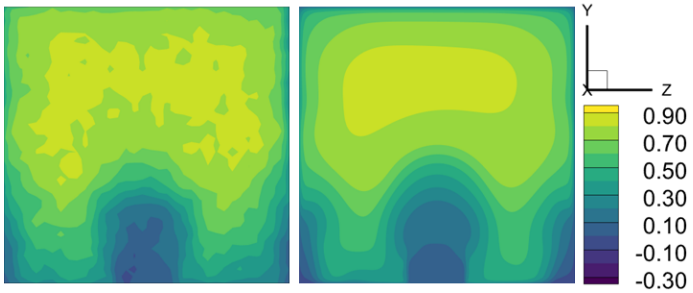

FIGURE 5: MRV (*L*) AND RANS (*R*) STREAMWISE VELOCITY CONTOURS FOR X-PLANE LOCATED AT THE CENTER OF INJECTOR

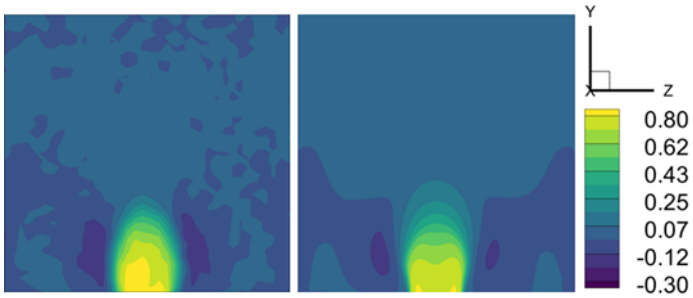

FIGURE 6: MRV (*L*) AND RANS (*R*) WALL NORMAL VELOCITY CONTOURS FOR X-PLANE LOCATED AT THE CENTER OF INJECTOR

FIGURE 7: MRV (*L*) AND RANS (*R*) SPANWISE VELOCITY CONTOURS FOR X-PLANE LOCATED AT THE CENTER OF INJECTOR

One means to conduct comparisons is to use the 3D nature of each data set. Velocity magnitudes are depicted for the MRV and RANS in Figure 8 at the 0.7 m/s level with slightly transparent solid surfaces included. This shows a relatively large volume with a partially hollow core, as this is above the averaged velocity within the test section. In this rendition the streamwise extent of each data set has included the region from the front cube to just past the last one to have similar total volume. In addition, the isosurfaces have each been made similarly translucent to aid in identifying the flow closer to the center region of the channel. It is possible to quantify the 3D volume of the velocity magnitude by creating a new binary variable that is positive when the velocity magnitude is 0.7 m/s or greater and integrating that variable over the volume. This integration was achieved using a built-in integration function included with TECPLOT software [14].

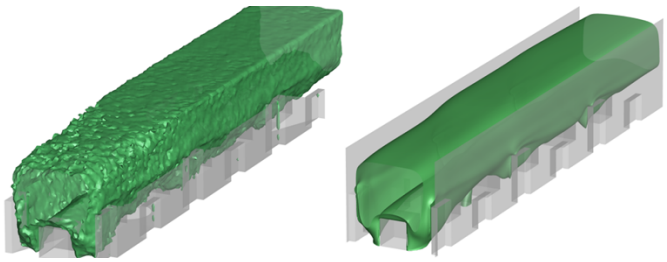

FIGURE 8: MRV (*L*) AND RANS (*R*) VELOCITY MAGNITUDE ISOSURFACES ≥ 0.7 M/S

The total volume of the test section encompassed by the data in Figure 8 is approximately 341,000 mm^3. The MRV isosurface volume from the figure integrates to 45,470 mm^3 or 13.3% of the total volume. The RANS data integrates to 40,355 mm^3 or 11.8% of the total volume. At least some of the visible differences occur near the corners of the field. This comparison of the isosurface volumes provides a quantitative metric involving significantly more data than the planar or line profile equivalents. However, the relatively large isosurface comparison in Figure 8 does not paint a clear picture of precisely where the data and simulations differ.

To improve comparisons of the type depicted in Figure 8, an isosurface of a single positive component of the vertical velocity is depicted in Figure 9. The value for this isosurface was selected where $V \geq 0.1$ m/s, as this is 20% of the bulk averaged velocity and highlights the vertical jet region of the flow field. Figure 9 suggests many similarities but also clear differences. The injector flow quickly interacts with the streamwise flow much like a jet in crossflow, and the extent it penetrates the mainstream could be of practical importance. In addition, the flow has strong vertical components as it interacts with the obstacles along the center plane and each side wall. The MRV shows increased vertical penetration into the free stream flow compared to the RANS. The top surfaces of each of the downstream obstacles after the injector site depicts vertical velocities in the RANS that all appear as slender cylinders at the front edge and look rectangular along the downstream side of the obstacle. In the MRV data, these differ going downstream, showing generally smaller volumes for each subsequent obstacle. The downstream volumes are also more spherical than the rectangular prisms in the RANS.

To better understand the injector flow performance differences, a region immediately downstream of the second and upstream of the third obstacles are cropped from the overall data. The lateral extent is limited to just beyond the obstacle width, and the vertical component limited to 1%–70% of *H*. This subregion is shown in Figure 10, with a velocity magnitude plane at y = 16mm to showcase the isosurface height difference. The MRV volume is this figure is 473 mm^3 while the RANS volume is 570 mm^3, a substantial difference (17%) for this specific region of the flow due in large part to the higher extent of the RANS isosurface as compared to the MRV. Further, when compared to the line profiles for the vertical velocity component at line 2, which have a high degree of similarity at the center of the injector, a remarkably different conclusion on volumetric agreement is obtained from the 3D comparison.

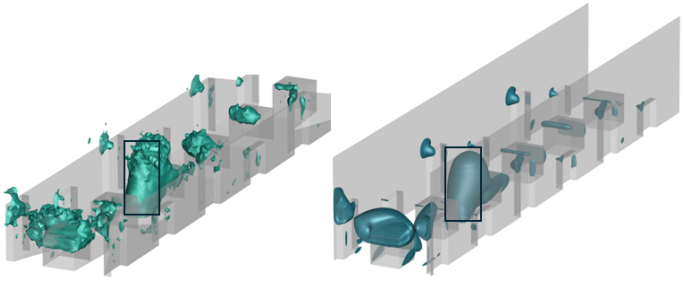

FIGURE 9: MRV (*L*) AND RANS (*R*) WALL NORMAL ISOSURFACES $V \geq 0.1$ M/S. BOXES INDICATE THE SUBREGIONS COMPARED IN FIGURE 10

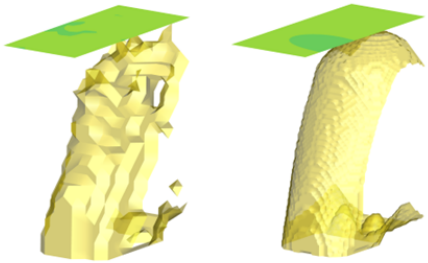

FIGURE 10: MRV (*L*) AND RANS (*R*) WALL NORMAL ISOSURFACES V ≥ 0.1 M/S FOR INJECTOR FLOW BETWEEN OBSTACLES

An additional isosurface that can be computed from the MRV measured data is the vorticity magnitude. Figure 11 depicts the vorticity magnitude for a subregion of the flow above a vorticity magnitude 300 1/s. The region consists of each of the center plane obstacles above the y = 0 plane but excludes side wall and top regions of the flow for clarity. The isosurface is colored by the velocity magnitude to extend the comprehension of the results. Of all the comparisons made so far, this is easily the most advanced because central differencing is used to extract vorticity from the measured three-component velocity in the experimental data. Using this vorticity magnitude threshold, the MRV isosurface volume is 1,735 mm^3, whereas the RANS has a volume of 1,253 mm^3, which is substantially less. The higher resolution of the RANS data is thought to contribute in part to the reduced volume in this comparison.

A final quantitative comparison is presented in Table 1. Table 1 uses Line 2, as well as the plane and volume depicted in Figure 2 to provide a side-by-side comparison of the three methods of comparison highlighted in this work – 1D, 2D, and 3D in nature. As the dimensionality increases, so do the number of points included in the metric, showcasing the opportunity to do multiple regional comparisons within complex areas of flow fields.

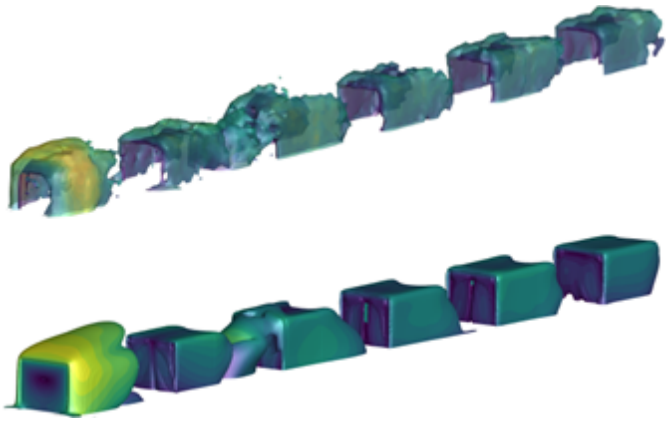

FIGURE 11: MRV (*T*) AND RANS (*B*) VORTICITY MAGNITUDE ISOSURFACES ≥ 300 1/S

TABLE 1. COMPARATIVE METRICS BETWEEN VELOCITY COMPONENTS FOR LINE 2, PLANE 2, AND VOLUME 2 IDENTIFED IN FIGURE 2.

	# of MRV points	# of RANS points	% RMSE σ/U_m
Line 2, U	24	24	11.6591
Line 2, V	24	24	8.4857
Line 2, W	24	24	2.6841
Plane 2, U	108	108	8.8996
Plane 2, V	108	108	7.0515
Plane 2, W	108	108	4.8169
Volume 2, U	864	864	9.8646
Volume 2, V	864	864	6.6926
Volume 2, W	864	864	5.0794

The results in Table 1 are presented in terms of the RMSE (defined in Equation 1) of the specific velocity component in comparison, normalized by the bulk mean velocity upstream of the obstacle array. Note that in this case, RMSE is computed at one location, i.e., N = 1, and the total of points M = 24, 108, and 864 for 1 line, 1 plane, and 1 volume, respectively. Prior to the comparison, the results from each set of data were down sampled onto a common grid with isotropic 2mm resolution, resulting in identical numbers of points and removing any requirement for weighting factors. The RMSE is largest for the streamwise and wall normal velocity components which are the largest velocity magnitudes involved. The spanwise velocity RMSE increases as the number of data points increases which sets it apart from the other two velocity components. It is likely this difference is because the centerline is where the spanwise velocity might be closest to zero whereas it increases away from the centerline as depicted in Figure 7. Velocities which may differ in sign between experiment and simulation do not suffer that penalty in the equation. In most cases, the RMSE % is larger than the quoted experimental uncertainty.

4. CONCLUSION

The inclusion of 3D comparisons between experiments and simulations is a validation activity achievable only with a subset of experimental methods. MRV data are readily available to be leveraged in a 3D approach, and they offer the potential to quantifiably assess simulation performance beyond simple 1D or 2D comparisons. The 3D data comparisons are especially important in critical regions such as near surfaces, between key features, or in areas with high gradients where differences could have significant impacts for design. MRV can enhance VVUQ efforts, and the use of discrete volumetric comparisons of measured or derived quantities in critical regions is one such means of improvement. Criteria may be established for volumetric regional agreement for such features as velocity component and velocity magnitude fields, vorticity and vorticity magnitude fields, or other derived quantities. Although using MRV data to conduct 3D comparisons should be conducted with care and requires additional details for validation activities, it is apparent that these activities should be pursued to ensure that simulations make substantive improvements leveraging their full field data.

ACKNOWLEDGEMENTS

The MRV data were measured at the Vanderbilt University Institute for Imaging Science (VUIIS) with the direct support of Drs. Saikat Sengupta and Jason Moore. In addition, the Director of the Center for Human Imaging at the institute, Dr. Seth Smith, is gratefully acknowledged for coordinating the MRI system scheduling and utilization.

REFERENCES

1. Raghava, A.K., et al., *A Probe for the Measurement of the Velocity Field.* Journal of Fluids Engineering, 1979. **101**(1): p. 143–146.
2. Adrian, R.J., *Particle-Imaging Techniques for Experimental Fluid Mechanics.* Annual Review of Fluid Mechanics, 1991. **23**(Volume 23, 1991): p. 261–304.
3. Westerweel, J., G.E. Elsinga, and R.J. Adrian, *Particle Image Velocimetry for Complex and Turbulent Flows.* Annual Review of Fluid Mechanics, 2013. **45**(Volume 45, 2013): p. 409–436.
4. Furnish, M.D., L.C. Chhabildas, and W.D. Reinhart, *Time-Resolved Particle Velocity Measurements at Impact Velocities of 10 km/s*, in *Conference: 1998 Hypervelocity Impact Symposium, Huntsville, AL (United States), 16–19 Nov. 1998; Other Information: PBD: [1998]*. 1998: United States. p. Medium: ED; Size: 16 p.
5. Bailey, S.C.C., et al., *Obtaining Accurate Mean Velocity Measurements in High Reynolds Number Turbulent Boundary Layers Using Pitot Tubes.* Journal of Fluid Mechanics, 2013. **715**: p. 642–670.
6. Kang, M., et al., *A Velocity Decomposition-Based 3D Optical Flow Method for Accurate Tomo-PIV*

Measurement. Experiments in Fluids, 2023. **64**(7): p. 135.
7. Elkins, C.J. and M.T. Alley, *Magnetic Resonance Velocimetry: Applications of Magnetic Resonance Imaging in the Measurement of Fluid Motion.* Experiments in Fluids, 2007. **43**(6): p. 823–858.
8. Benson, M.J., et al., *The 2019 MRV Challenge: Turbulent Flow through a U-Bend.* Experiments in Fluids, 2020. **61**(6): p. 148.
9. Bruschewski, M., et al., *Commissioning of an MRI Test Facility for CFD-Grade Flow Experiments in Replicas of Nuclear Fuel Assemblies and Other Reactor Components.* Nuclear Engineering and Design, 2021. **375**: p. 111080.
10. Markl, M., et al., *Time-Resolved Three-Dimensional Phase-Contrast MRI.* Journal of Magnetic Resonance Imaging, 2003. **17**(4): p. 499–506.
11. in *Guide: Guide for the Verification and Validation of Computational Fluid Dynamics Simulations (AIAA G-077-1998(2002))*.
12. Benson, M.J., et al., *MRV Challenge 2: Phase Locked Turbulent Measurements in a Roughness Array.* Experiments in Fluids, 2023. **64**(2): p. 28.
13. Software, S.D.I., *Simcenter STAR-CCM+, v. 2024.1*. Siemens 2024.
14. Software, *TECPLOT 360 EX R1*. 2023.